

# Semiconducting character in Ruddlesden-Popper bilayer nickelate $\text{Y}_{0.5}\text{Sr}_{2.5}\text{Ni}_{2-x}\text{Al}_x\text{O}_7$

H. Yilmaz,<sup>1,\*</sup> P. Sosa-Lizama,<sup>2</sup> M. Knauff,<sup>2</sup> K. Küster,<sup>2</sup> U. Starke,<sup>2</sup>  
M. Isobe,<sup>2</sup> O. Clemens,<sup>1</sup> P. A. van Aken,<sup>2</sup> Y. E. Suyolcu,<sup>2</sup> and P. Pupal<sup>2,3,†</sup>

<sup>1</sup>University of Stuttgart, Institute for Materials Science,

Materials Synthesis Group, Heisenbergstraße 3, 70569 Germany

<sup>2</sup>Max Planck Institute for Solid State Research, Heisenbergstraße 1, 70569 Stuttgart, Germany

<sup>3</sup>2nd Physics Institute, University of Stuttgart, 70569 Stuttgart, Germany

(Dated: March 12, 2025)

With the discovery of superconductivity under pressure in the Ruddlesden-Popper (RP) bilayer  $\text{La}_3\text{Ni}_2^{2.5+}\text{O}_7$  and trilayer  $\text{La}_4\text{Ni}_3^{2.66+}\text{O}_{10}$ , a new field of nickelate superconductors opened up. In this respect, Sr-Ni-O RP-type phases represent alternative systems that exist with partial cation substitution. We demonstrate that by Y-doping in  $\text{Sr}_3\text{Ni}_{2-x}\text{Al}_x\text{O}_7$  (SNAO), as  $\text{Y}_y\text{Sr}_{3-y}\text{Ni}_{2-x}\text{Al}_x\text{O}_7$  (YSNAO), the drawback of an insulating ground state is overcome, and a significant decrease in resistivity is achieved with crystals exhibiting semiconducting behavior. Using extensive diffraction and spectroscopy, as well as transport and magnetization measurements, the structural, chemical, electrical, and magnetic properties of the as-grown and reduced compounds were investigated. In the Al-free growth, a known  $n = 1$  RP system with  $\text{Sr}_{1.66}\text{Y}_{0.33}\text{NiO}_{4-\delta}$ , from which the first single crystals were obtained, was further confirmed, opening the door for future exploration of  $A$ -site substituted RP-type phases without Ni-site disorder.

## I. INTRODUCTION

Nickelates provide an emerging platform for oxide superconductors with various structural *motifs*: moving from hole-doped rare-earth (*RE*) infinite-layer structures in  $\text{RENiO}_2$  [1], to reduced RP  $\text{Nd}_6\text{Ni}_5\text{O}_{12}$  [2], to undoped RP-type phases under pressure.  $\text{La}_3\text{Ni}_2\text{O}_7$  was found to show filamentary superconductivity both in the bilayer [3] and in the new structural polymorph monolayer-trilayer variant [4]. Later on, also  $\text{La}_4\text{Ni}_3\text{O}_{10}$  [5] and  $\text{La}_2\text{PrNi}_2\text{O}_7$  [6] were shown to bulk superconduct. In these RP-type phases, the superconductivity occurs at similar pressures of around 15 GPa, accompanied by a structural transition from an orthorhombic to a tetragonal system. The RP series denotes structural building blocks in oxide systems consisting of alternating rock-salt and perovskite layers with the composition  $A_{n+1}T_n\text{O}_{3n+1}$ , where  $n$  is the number of consecutive  $\text{TO}_6$  perovskite blocks within a structural unit. Tetragonal  $I/4mmm$  RP-type phases are known for Sr on the  $A$ -site with different  $3d$  or  $4d$  transition metal ions [7–16]. With  $A = \text{Sr}$ , the series implies the presence of a 4+ oxidation state for the  $T$ -cations under a stoichiometric oxygen content. Due to the flexibility of the oxidation state of transition metals, a reduction down to  $\text{Sr}_3\text{T}_2\text{O}_5$  is possible for certain compounds [17]. Similarly, the  $A$ -site can be substituted by rare-earths [18], leading to a lower oxidation state of the  $T$  cation. However, only for  $T = \text{Ni}$  a full  $A = \text{La}$  phase is reported for the whole RP-type phases [19], leading to different oxidation states varying with  $n$ . In contrast, the Sr-bearing series has been much less studied, leaving room for its exploration and the possibility of stabilizing an ambient pressure superconductor.

Here, Y-doping in the  $A$ -sites, i.e.,

$\text{Y}_y\text{Sr}_{3-y}\text{Ni}_{2-x}\text{Al}_x\text{O}_7$ , is utilized, and a unique crystal formation exhibiting a tetragonal structure without external pressure is examined, which is structurally analogous to recently established RP-type  $n = 2$  single crystals for Sr-Ni-O with Al-substitution (SNAO) [20]. Unlike  $\text{Sr}_3\text{Ni}_{2-x}\text{Al}_x\text{O}_7$ , with Y-doping transitions occurred solely between stable RP phases with varying  $n$ . Notably, by leveraging  $\text{Y}^{3+}$  doping, conductivity is drastically increased by a factor of  $10^6$ . While X-ray diffraction (XRD) and scanning transmission electron microscopy (STEM) measurements prove the structural quality of these crystals, X-ray photoemission spectroscopy (XPS) experiments combined with thermogravimetric analysis (TGA) reveal an extraordinarily high oxidation state  $\text{Ni}^{4+}$ . Additionally, upon topochemical oxygen reduction, depending on the doping content, reduced phases of  $\text{Ni}^{2+}$ ,  $2.33$ ,  $2.66+$  can be reached.

## II. METHODS

The experimentally obtained crystal structure was analyzed using Density functional theory (DFT). DFT calculations were performed using the scalar-relativistic implementation of the full-potential local orbital (FPLO) code [21], version 22.00-62. Self-consistency was achieved when the change in total energy between subsequent steps was less than  $10^{-8}$  Hartree. The exchange-correlation potential was parametrized as described by Perdew and Wang [22] and the Brillouin zone integration carried out on regular meshes chosen such that the total energy was converged to better than 1 meV. The phase diagram was constructed by calculating the formation energy based on references of the elemental solids of Sr, Ni and  $\text{O}_2$ . Experimental crystal structures were taken

from the Inorganic Crystal Structure Database (ICSD) [23–30]. For the case of  $\text{Sr}_2\text{NiO}_4$  and  $\text{Sr}_3\text{Ni}_2\text{O}_7$ , we started from the experimentally determined structures (Ref. [31] and present work) with doping and manually removed dopants to simulate the parent compound. For  $\text{Sr}_9\text{Ni}_7\text{O}_{21}$ , the partially occupied oxygen ions were moved to the high symmetry site of the structure reported in Ref. [32]. The algorithm for the convex hull is implemented in the atomic simulation environment (ASE) [33].

The aim of synthesis is to grow differently Y doped  $\text{Sr}_3\text{Ni}_2\text{O}_7$  crystals, where co-doping of Al is necessary [20], which is achieved by preparing different precursor phases and performing floating zone growth. For the aimed  $\text{Y}_y\text{Sr}_{3-y}\text{Ni}_{2-x}\text{Al}_x\text{O}_7$  crystals, the optical floating zone (OFZ) technique was used under 9 bar oxygen partial pressure. First, feed rods were prepared by the conventional Solid-State method using stoichiometric amounts of  $\text{Y}_2\text{O}_3$  (Alfa Aesar, 99.995%),  $\text{SrCO}_3$  (Sigma Aldrich, 99.995%), NiO (Alfa Aesar, 99.998%), and  $\text{Al}_2\text{O}_3$  (Alfa Aesar, 99.995%). The precursor powders were mixed using a ball mill and sintered in an aluminum oxide crucible at 1100 °C for 12 hours in air. The as-sintered powders were formed into cylindrical rods ( $\phi=4$  mm;  $l=100$  mm) by an isostatic press (70 MPa) using rubber forms and subsequently annealed at 1200 °C 12 hours in air. The rod was installed in a conventional four mirror lamp Optical Float Zone Furnace (FZ-T-10000-H-III-VPR). Finally, single crystal growth was conducted with  $4\times 1000$  W halogen lamps. During the growth process, the feed and seed rods were counter-rotated (24 rpm) in order to minimize the diffusion zone close to the crystallization surface. Oxygen gas flow (100 cc/min) was applied, and an auxiliary pressure of 9 bar was simultaneously introduced to stabilize the highly oxidized phase. To obtain relatively large single crystals, the growth rate was kept at 4 mm/h. Post-growth, the boule was cracked using a mortar, and single crystals were selected for further analysis.

The crystallinity and phase purity of the as-grown single crystals were examined by XRD on powdered samples. Powder X-ray diffraction (PXRD) measurements were performed on ground crystals in order to investigate the presence of impurities as well as to determine the crystal structure and lattice parameters. XRD patterns were recorded at room temperature using a Rigaku Miniflex diffractometer with Bragg-Brentano geometry, Cu  $K_\alpha$  radiation, and a Ni filter. Rietveld refinements were carried out with TOPAS V6 software. Single crystal diffraction was performed at room temperature using a Rigaku XtaLAB mini II instrument with Mo  $K_\alpha$  radiation. Data were analyzed with CrysAlis (Pro), and the final refinement was performed using Olex2 with SHELX. Energy-dispersive X-ray spectra (EDX) were recorded with a NORAN System 7 (NSS212E) detector in a TESCAN Vega SEM (TS-5130MM). On each crystal, dozens

of points were analyzed, and the standard deviation was considered as an error. The STEM lamellae were prepared by thinning the crystal specimen down to electron transparency via Focused Ion Beam milling with Ga ions on a Thermo Fisher Scios II FIB using the liftout method. The lateral dimensions of the specimen were  $12 \times 10$   $\mu\text{m}$ , with an overall thickness below 100 nm. In the analyzed regions of the samples, the thickness was  $\sim 50$  nm determined by the Fourier log-ratio method. High-resolution STEM imaging was performed with a JEOL JEM-ARM200F equipped with a cold field-emission electron source and a probe  $C_s$ -corrector (DCOR, CEOS GmbH), at an acceleration voltage of 200 kV. The STEM-HAADF acquisition was carried out with a convergence (semi-) angle of 28 mrad, resulting in a probe size of  $\sim 0.8$  Å. Collection angles for HAADF images were 75 to 310 mrad. XPS measurements were carried out at a Kratos Axis Ultra with a monochromated Al  $K_\alpha$  X-ray source. The small crystals were glued on a dedicated sample holder with pillars (with a diameter smaller than the single crystals) in order to avoid signals from the environment. The samples were transferred under inert gas into the XPS system without exposure to air. A charge neutralizer was used to compensate for surface charging, and the binding energy was calibrated to C 1s at 284.8 eV (adventitious carbon). The data was analyzed using Casa XPS V2.3.26rev1 [34] and the peaks were fitted with a LA (Gaussian and Lorentzian convolution) line shape after Shirley background subtraction for the quantification. Differential Thermal Analysis (DTA) and Thermo gravimetry Analysis (TGA) were performed using a Netzsch DTA/TG. Magnetic susceptibility measurements were conducted using a vibrating sample magnetometer (MPMS 3, Quantum Design), and the electrical transport measurements were carried out using a Physical Property Measurement System (PPMS, Quantum Design).

### III. RESULTS

Motivated by our previous synthesis of  $n = 2$  Sr-based RP nickelates via successful Al substitution in SNAO [20], simple DFT calculations for the Al free RP  $n = 2$   $\text{Sr}_3\text{Ni}_2\text{O}_7$  case were performed based on experimental structure results with Al crystallizing in the tetragonal  $I4/mmm$  structure. The results are displayed in Fig. 1 a) with individual d orbitals colorcoded. Notably, the overall bandstructure is (not surprisingly) extremely similar to bilayer  $\text{La}_3\text{Ni}_2\text{O}_7$  under external pressures of 29.5 GPa [35] besides an enormous shift of the Fermi energy of 1 eV down due to the overall strong doping realized with  $\text{Sr}^{2+}$  on the A-site. Here, however without external pressure application a tetragonal structure is realized and with successful electron doping a similar superconductor could be created. DFT results indicate a metal with

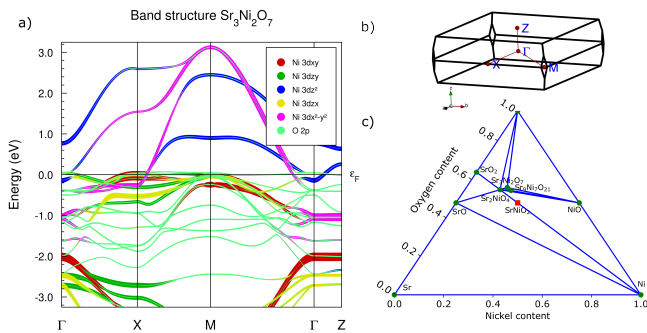


FIG. 1. a) Orbital-projected band structure for Ni 3d- and O 2p-orbitals calculated by DFT. b) High-symmetry path in the Brillouin zone of  $\text{Sr}_3\text{Ni}_2\text{O}_7$ . c) Ternary phase diagram of Sr-Ni-O<sub>2</sub> based on stability calculations. Stable (unstable) phases are marked as green (red) points.

multiple bands crossing the Fermi level. These bands are primarily from Ni- $d_z^2$  and Ni- $d_{x^2-y^2}$  orbitals. In addition, various flat bands of Ni- $d_{xy}$  and Ni- $d_{xz}$  exist at the Fermi level. This DFT picture is insufficient due to the strong electronic correlations of Ni- $d$  electrons, but gives a first insight into this new candidate of Nickelate superconductor. The latter could be realized in future via doping pure  $\text{Sr}_3\text{Ni}_2\text{O}_7$  with hope at ambient pressure superconductivity from the already tetragonal structure. This is experimentally easier achieved in bulk samples than for La the system, as the latter is already distorted with full oxidization [4] and any doping and hence substitution would increase this distortion as unlike external pressure this is always realized by chemical pressure [36], unlike thin films, which can via epitaxy influence the bond angle [37].

Furthermore, stability calculations have been performed for the Sr-Ni-O phase diagram as shown in Fig. 1 c). While the binary phase diagram [20, 38] only reveal  $\text{Sr}_9\text{Ni}_7\text{O}_{21}$ , which we also found as the stable phase for a "Sr<sub>3</sub>Ni<sub>2</sub>O<sub>7</sub>" OFZ growth at 10 bar O<sub>2</sub>, calculations indicate a general stability of the simple RP  $n = 2$   $\text{Sr}_3\text{Ni}_2\text{O}_7$  and RP  $n = 1$   $\text{Sr}_2\text{NiO}_4$ . Notably, this does not yield the experimental conditions to realize this phase and as showed before, Al substitution stabilizes the RP  $n = 2$  phase [20]. Interesting is also the stability of  $n = 1$  in the course of this work as it could be stabilized by simple A-site substitution, without the disadvantage of co-doping the Ni-site.

In this work, the effect of electron doping was extensively explored by introducing Y into the structure as  $\text{Y}_y\text{Sr}_{3-y}\text{Ni}_{2-x}\text{Al}_x\text{O}_{7-\delta}$  (YNAO). The crystals are grown after the preparation of stoichiometric powders, as described in the methods section. First, a greater doping with  $y = 1$  was attempted with the established content of substitutional Al,  $x = 0.25$ . Here, the growth required large feeding rates but otherwise realized a stable optical floating zone process. However, the obtained boule

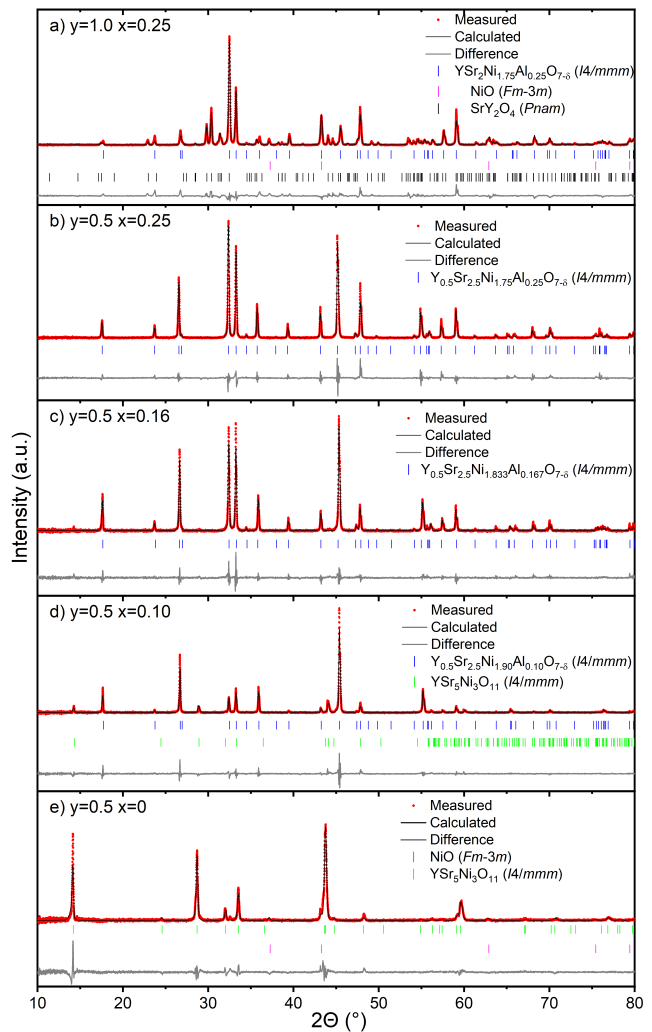


FIG. 2. Rietveld fit of the room-temperature PXRD pattern of  $\text{Y}_y\text{Sr}_{3-y}\text{Ni}_{2-x}\text{Al}_x\text{O}_{7-\delta}$ . For each plot, the solid black line corresponds to the calculated intensity from the Rietveld refinement, the solid gray line is the difference between the experimental and calculated intensities, and the vertical blue/green bars are the calculated Bragg peak positions.

revealed a phase mix, as visible via the PXRD results shown in Figure 2 a), and contained only small crystals of sub-millimeter size. Most importantly, the  $n = 2$  RP-type phase formed as the main phase, with reduced lattice constants (see Table I) as expected from the smaller Y ions (see Table I). Additionally, the Y solubility limit was reached as visible from the presence of a Y-rich impurity phase of the spinel phase  $\text{SrY}_2\text{O}_4$  (see Figure 2 a) and Table I) with 22.98(14) wt%. As the boule contained shiny single crystals regardless of the presence of impurity phases, the stoichiometry was analyzed by EDX and found to be  $\text{Y}_{0.47(5)}\text{Sr}_{2.56(3)}\text{Ni}_{1.78(8)}\text{Al}_{0.27(2)}\text{O}_{6.5(7)}$ . The next step was a growth with  $x = 0.25$  and  $y = 0.5$  under the same conditions as described in the methods section. The process required only subtle feeding, and

TABLE I. Result of Rietveld powder refinement. Listed are the attempted or nominal composition, with their substitution content for Y ( $y$ ) and Sr ( $x$ ), the RP-type phase  $n$ , the relative wt%, the lattice parameters  $a, b, c$  and the Nickel oxidation state from XPS results for different float zone growths and hydrogen-treated phases.

Attempted Comp.	$y$	$x$	RP $n$	wt%	Cell	$a$ [Å]	$b$ [Å]	$c$ [Å]	Ni $^{2+}$
$\text{Sr}_3\text{Ni}_{1.75}\text{Al}_{0.25}\text{O}_{7-\delta}$	0	0.25	2	100	$I4/mmm$	3.8020(5)	3.8020(5)	20.2616(3)	3.85
$\text{YSr}_2\text{Ni}_{1.75}\text{Al}_{0.25}\text{O}_{7-\delta}$	1	0.25	2	72.38(18)	$I4/mmm$	3.79089(6)	3.79089(6)	19.8549(4)	
$\text{Y}_{0.5}\text{Sr}_{2.5}\text{Ni}_{1.75}\text{Al}_{0.25}\text{O}_{7-\delta}$	0.5	0.25	2	100	$I4/mmm$	3.78842(3)	3.78842(3)	19.99846(16)	3.93
$\text{Y}_{0.5}\text{Sr}_{2.5}\text{Ni}_{1.833}\text{Al}_{0.166}\text{O}_{7-\delta}$	0.5	0.166	2	100	$I4/mmm$	3.79113(4)	3.79113(4)	19.92860(18)	
$\text{Y}_{0.5}\text{Sr}_{2.5}\text{Ni}_{1.90}\text{Al}_{0.10}\text{O}_{7-\delta}$	0.5	0.1	2	90.0(4)	$I4/mmm$	3.79112(5)	3.79112(5)	19.9151(2)	
$\text{Y}_{0.5}\text{Sr}_{2.5}\text{Ni}_{1.90}\text{Al}_{0.10}\text{O}_{7-\delta}$	0.5	0.1	1	10.0(4)	$I4/mmm$	3.7887(17)	3.7887(17)	12.2871(3)	
$\text{Y}_{0.5}\text{Sr}_{2.5}\text{Ni}_2\text{O}_{7-\delta}$	0.5	0	1	77.5(11)	$I4/mmm$	3.76333(15)	3.76333(15)	12.3791(3)	
$\text{Sr}_3\text{Ni}_{1.75}\text{Al}_{0.25}\text{O}_{5+\delta}$	0	0.25	2	100	$Immm$	3.603(2)	3.839(3)	20.442(14)	
$\text{Y}_{0.5}\text{Sr}_{2.5}\text{Ni}_{1.75}\text{Al}_{0.25}\text{O}_{5+\delta}$	0.5	0.25	2	100	$Immm$	3.5506(4)	3.8490(4)	20.254(2)	
$\text{Y}_{0.5}\text{Sr}_{2.5}\text{Ni}_{1.833}\text{Al}_{0.166}\text{O}_{5+\delta}$	0.5	0.166	"2	100	$Immm$	3.51772(5)	3.85059(7)	20.2461(4)	

the melt was extremely stable. Upon tapping of the obtained boule, crystals of several mm in length broke apart. For this case, PXRD in Figure 2 b) reveals a pure  $n = 2$  RP-type phase, with the corresponding lattice constants summarized in Table I. This is further confirmed by the exact stoichiometric result of EDX, indicating  $\text{Y}_{0.51(6)}\text{Sr}_{2.52(3)}\text{Ni}_{1.74(2)}\text{Al}_{0.26(4)}\text{O}_{6.7(2)}$ . Moreover, due to the homogeneous crystals obtained, it was motivated to both reduce the Al-disorder in the Ni lattice and enhance the electric conductivity by a growth of  $y = 0.5$  and  $x = 0.166$ . PXRD of the grown crystals are shown in Figure 2 c), once more revealing a pure  $n = 2$  RP-type phase, though with slightly smaller single crystals than in the previous case.

In addition, after a successful growth with a reduced Al content, another growth was conducted without Al, maintaining the same Y content,  $y = 0.5$  and  $x = 0$ . Similarly, the growth was stable with the required feeding but resulted in a phase mix. PXRD analysis in Figure 2 e) revealed a major formation of the defect RP  $n = 1$ -type phase  $\text{Y}_{0.33}\text{Sr}_{1.66}\text{NiO}_{3.75}$  (or  $\text{YSr}_5\text{Ni}_3\text{O}_{11}$  [31, 39]) with 73.0(9) wt%. Finally, an intermediate Al-concentration was attempted with  $y = 0.5$  and  $x = 0.1$ , still yielding a phase mix. This time it consists of  $n = 1$  and  $n = 2$ , as visible in the PXRD in Figure 2 d). The major phase here, however is  $n = 2$  with 90%, as summarized in Table I, with a slightly reduced  $c$ -axis in comparison to  $x = 0.166$ . Due to the inter-growth of two phases, the crystal size is slightly reduced, but the two phases of crystals can be clearly distinguished in single crystalline form. The EDX result on the obtained  $n = 2$  crystals revealed a perfect stoichiometry of  $\text{Y}_{0.55(1)}\text{Sr}_{2.52(2)}\text{Ni}_{1.83(6)}\text{Al}_{0.16(8)}\text{O}_{6.6(4)}$ . Notably, following Vegard's law, an extrapolation from  $x = 0.25$  and 0.166 of the  $c$ -axis compression hints at a solubility limit below the stoichiometry of  $\text{Y}_{0.5}\text{Sr}_{2.5}\text{Ni}_{1.85}\text{Al}_{0.15}\text{O}_{7-\delta}$  for the  $x = 1$  case. Hence, the phase diagram of YSAO can be drawn as depicted in Figure 3, where the transitions occur only between the RP-type phases when Y is

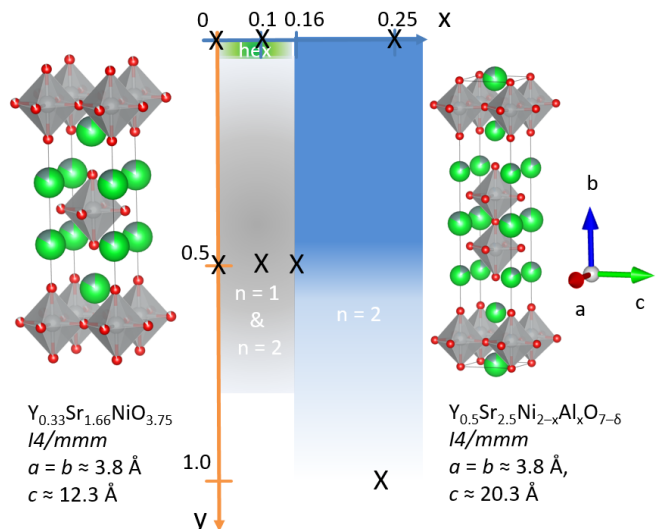


FIG. 3. Chemical stability of the  $\text{Y}_y\text{Sr}_{3-y}\text{Ni}_{2-x}\text{Al}_x\text{O}_7$  series, with the Al (Y) content  $x$  ( $y$ ) as the horizontal (vertical) axis. At the axis, i.e. with finite  $y$  at  $x = 0$ , the defect Ruddlesden-Popper  $n = 1$  type-phase  $\text{Y}_{0.33}\text{Sr}_{1.66}\text{NiO}_{3.75}$  (or  $\text{YSr}_5\text{Ni}_3\text{O}_{11}$ ) and NiO are formed. For  $0 < x < 0.16$  and  $0.5 < y \leq 1$  (grey region), a mixture of the two phases is found. Notably, the narrow green stripe marks the Y-free area, where  $\text{Sr}_9\text{Ni}_7\text{O}_{21}$  is the phase mixing with  $n = 2$  [20], while in the blue range, phase pure  $n = 2$  RP-type  $\text{Y}_{0.5}\text{Sr}_{2.5}\text{Ni}_{2-x}\text{Al}_x\text{O}_7$  is obtained (see Figure 2).

introduced to the system.

For the phase pure  $\text{Y}_{0.5}\text{Sr}_{2.5}\text{Ni}_{1.75}\text{Al}_{0.25}\text{O}_{7-\delta}$  crystal, the boule and single crystal images are shown in Figure 4 a,b,c and d. The single-crystal diffraction refinement results corresponding to the zonal maps are summarized in Table II. Moreover, the structural quality of the crystal was verified on the nanoscale with scanning transmission electron microscopy (STEM) imaging. STEM high-angle annular dark field (HAADF) images at increasing magnifications show a clean, defect-free sample in Figure 4 e-g. The higher-magnification image in Figure 4 g) exempli-

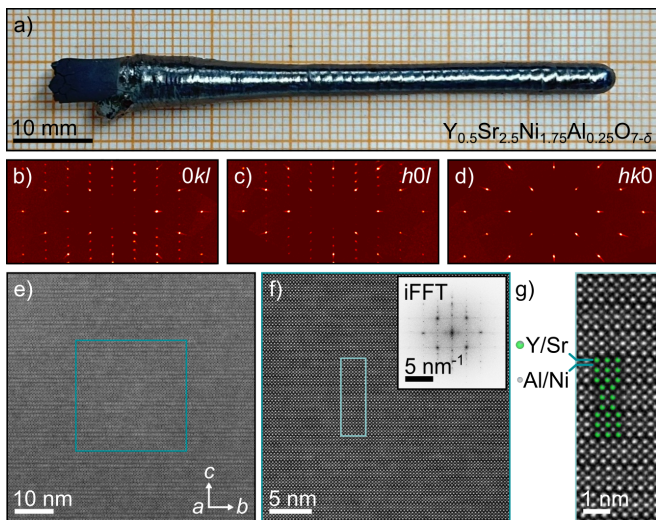


FIG. 4. a) Picture of the OFZ grown boule of  $Y_{0.5}Sr_{2.5}Ni_{1.75}Al_{0.25}O_{7-\delta}$ , and its single crystal XRD zonal maps along b)  $0kl$ , c)  $h0l$  and d)  $hk0$ . e) Overview STEM-HAADF image of a region of  $64 \times 64$  nm from the same crystal shows a defect-free sample. f) High-magnification image showing the presence of a single stacking order, consisting of bilayer perovskite slabs. The inset corresponds to the iFFT of the image in e), analogous to b). g) Enlarged region within f) shows the clear RP-type  $n = 2$  stacking, where the larger (smaller) intensity spots correspond to atomic columns of Sr/Y (Ni/Al). The structural model is overlaid for reference.

TABLE II. Refined atomic coordinates of  $Y_{0.5}Sr_{2.5}Ni_{1.75}Al_{0.25}O_{7-\delta}$  in the tetragonal  $I4/mmm$  (#139) structure, extracted from single crystal XRD. The corresponding lattice constants and quality parameters are:  $a = 3.8045(4)$  Å,  $c = 19.964(3)$  Å;  $R1 = 0.0501$ ,  $wR2 = 0.1659$ ,  $GOF = 1.222$

Atom	Site	x	y	z	Occ	Uiso
Y	Y01	1/2	1/2	0.18217(11)	0.167	0.0095(8)
Sr	Sr01	1/2	1/2	0.18217(11)	0.833	0.0095(8)
Y	Y02	0	0	1/2	0.167	0.0194(10)
Sr	Sr02	0	0	1/2	0.833	0.0194(10)
Ni	Ni03	1/2	1/2	0.40299(16)	0.875	0.0077(9)
Al	Al03	1/2	1/2	0.40299(16)	0.125	0.0077(9)
O	O004	1/2	1/2	1/2	1	0.10(2)
O	O005	1/2	1/2	0.3065(9)	1	0.015(4)
O	O006	1/2	0	0.4112(7)	1	0.033(4)

ifies the presence of the observed single RP-type phase ( $n = 2$ ) throughout the sample. Moreover, the inverted Fast Fourier Transform (iFFT) taken over the larger field-of-view shows the spatial frequencies consistent with the extinction rules for the  $I4/mmm$  space group, which is in agreement with the  $(0kl)$  XRD map (cf. Figure 3b). Atomic columns of different sizes are observed when comparing  $A$ - and  $T$ -sites, with the former (Sr/Y) larger than the latter (Ni/Al), in accordance with the atomic number contrast of STEM-HAADF.

To confirm the remarkably high nominal oxidation

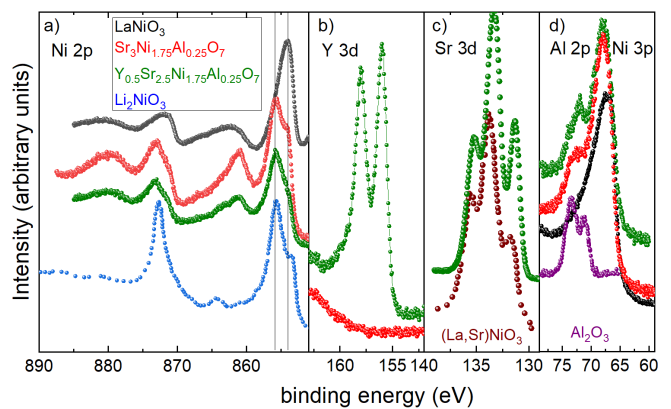


FIG. 5. XPS spectra of  $LaNiO_3$  [40] (black), SNAO [20] (red) and  $Y_{0.5}Sr_{2.5}Ni_{1.75}Al_{0.25}O_{7-\delta}$  (green) for mutual comparison. These are displayed in the energy ranges corresponding to the binding energies of a) Ni  $2p$ , b) Y  $3d$ , c) Sr  $3d$  and d) Al  $2p$  states. The XAS spectrum of  $Li_2NiO_3$  [41] is shown for reference.

state in the doped system, XPS analyses were used. The corresponding results are displayed in Figure 5, where spectra within the relevant binding energies are shown for a) Ni  $2p$ , b) Y  $3d$ , c) Sr  $3d$ , and d) Al  $2p$ . In the Ni case, the strongest peak appears at 855.6 eV, originating from  $Ni^{4+}$ . A shoulder at 854.0 eV is visible as well, where both are indicated by a vertical line. Here, the shoulder is more intense compared to the one in the reference  $Li_2NiO_3$  XAS spectrum [41]. Moreover, since this feature appears at a similar binding energy to that of the main peak in  $LaNiO_3$ , which contains  $Ni^{3+}$ , it could be inferred that a small amount of  $Ni^{3+}$  was present in the SNAO crystals. More precisely, by fitting two peaks to this double structure and comparing their relative areas, an estimated composition of 15%  $Ni^{3+}$  and 85%  $Ni^{4+}$  was determined for SNAO. Similarly,  $Sr_{2.5}Y_{0.5}Ni_{1.85}Al_{0.15}O_{7-\delta}$ , the Ni  $2p$  spectra has the same character as for SNAO, but a slightly weaker feature is associated with  $Ni^{3+}$  (at 854 eV). In this case, the same fitting method leads to 7% of  $Ni^{3+}$ , which gives a nominal oxygen amount of 7.06 (i.e.,  $\delta = -0.06$ ), confirming the absence of oxygen vacancies in YSNAO. Notably, the reference  $Li_2NiO_3$  and the XPS data differed by the presence of an additional satellite around 861 eV, which was attributed to a residual amount of decomposing hydroxides on the examined samples' surfaces. In Figure 5 b), for Y  $3d_{5/2}$  and  $3d_{3/2}$ , the expected two spin-orbit split peaks were observed at 156 and 158 eV, respectively, corresponding to its 3+ oxidation state [42]. For the Sr  $3d$  case shown in Figure 5 c), two doublets appear: first at the Sr  $3d_{5/2}$  binding energy, at 131.5 eV, then at 133.5 eV. The latter can be related to the instability of Sr on the surface, probably reacting to form Sr-oxide or hydroxide [43]. The spectra is very similar to that of perovskite  $(La,Sr)NiO_3$  single crystals [40]. Notably, the Al  $2p$  lines (with  $Al_2O_3$  as

a reference [44]) are slightly better resolved for YSNAO sample, as visible in Figure 5 d), but their overlap with Ni 3*p* features makes a clear analysis impossible.

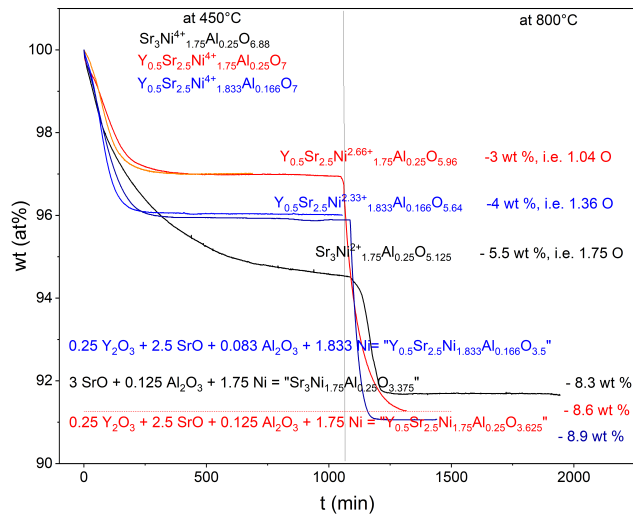


FIG. 6. TGA analyses of the  $\text{Y}_{0.5}\text{Sr}_{2.5}\text{Ni}_{1.75}\text{Al}_{0.25}\text{O}_{7-\delta}$  (red and orange shown for reproducibility),  $\text{Y}_{0.5}\text{Sr}_{2.5}\text{Ni}_{1.833}\text{Al}_{0.166}\text{O}_{7-\delta}$  (two blue lines for showing reproducibility) and  $\text{Sr}_3\text{Ni}_{1.75}\text{Al}_{0.25}\text{O}_{7-\delta}$  (black) [20] single crystals, heated at 450°C (left) and 800°C (right) in Ar/5%H<sub>2</sub> flow, plotted versus time.

After phase-pure crystals were established with  $y = 0.5$  and  $x = 0.166, 0.25$ , their structural motif was modified by topochemical hydrogen reduction. Conventional TGA measurements were employed, and the phases were reduced in two steps, the results of which are displayed in Figure 6. First, the crystals were heated to 450°C in 5% hydrogen until a plateau was reached, hence a stable intermediate oxidation state. Next, the temperature was increased to 800°C in order to fully decompose the species and reach metallic Ni. From the full reduction, the as-grown oxygen content was estimated via the mass loss. It was found that, for all phases, full oxidation was reached, and the Y variants exhibited no oxygen deficiency ( $\delta \approx 0$ ) in line with the XPS result even indicating an oxidation state of Ni beyond O<sub>7</sub>. Besides, different oxidation states were observed upon reduction, depending on the doping concentration. For the already reported SNAO, a Ni<sup>2+</sup> reduced phase stabilizes with a mass loss of 1.75 oxygen, i.e. 5.5 wt% [20]. For the  $\text{Y}_{0.5}\text{Sr}_{2.5}\text{Ni}_{1.85}\text{Al}_{0.15}\text{O}_{7-\delta}$  a mass loss of 3 wt% was observed, corresponding to 1.04 oxygen, thereby reaching a stable Ni<sup>2.66+</sup> state. Finally, for the optimized growth, further reduction of  $\text{Y}_{0.5}\text{Sr}_{2.5}\text{Ni}_{1.833}\text{Al}_{0.166}\text{O}_{7-\delta}$  resulted in a mass loss of 4 wt%, corresponding to 1.36 oxygen, which results in a stable Ni<sup>2.33+</sup> state. For all reduced phases, the same orthorhombic crystal structure previously reported for SNAO [20] was observed, where the in-plane oxygen removal was best captured by the reduc-

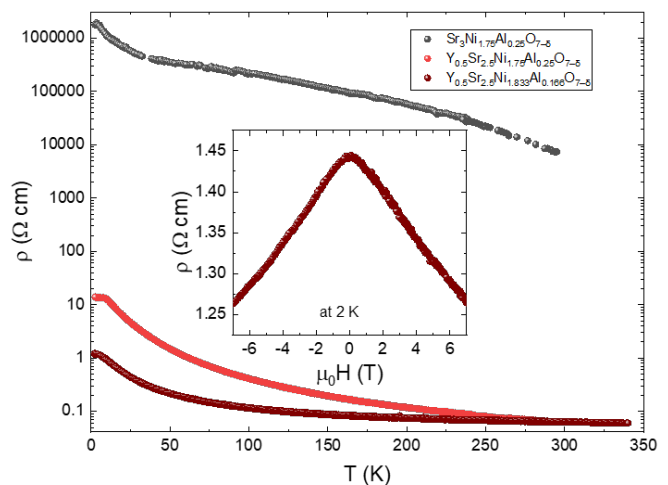


FIG. 7. Electrical transport for YSNAO. Shown are the resistivity of  $\text{Sr}_3\text{Ni}_{1.75}\text{Al}_{0.25}\text{O}_{7-\delta}$  (black),  $\text{Y}_{0.5}\text{Sr}_{2.5}\text{Ni}_{1.75}\text{Al}_{0.25}\text{O}_{7-\delta}$  (red) and  $\text{Y}_{0.5}\text{Sr}_{2.5}\text{Ni}_{1.833}\text{Al}_{0.166}\text{O}_{7-\delta}$  (brown) versus temperature in the range between 1.8 and 300 K. As an inset, the magnetoresistance of  $\text{Y}_{0.5}\text{Sr}_{2.5}\text{Ni}_{1.833}\text{Al}_{0.166}\text{O}_{7-\delta}$  is shown under fields varying from -7 to 7 T, at a temperature of 2 K.

tion of the lattice constant,  $a$  (see Table I).

Finally, the electrical properties of the novel RP-type nickelate crystals were measured. Figure 7 presents the resistivity of three crystals, where SNAO exhibits semi-conducting behavior with a wide bandgap [20]. With the introduction of  $y = 0.5$  amount of Y to the compound, a drastic reduction in the resistivity by six orders of magnitude was observed. Similarly, when reducing the amount of Al from  $x = 0.25$  to  $x = 0.166$ , the resistivity at room temperature was nearly unchanged but reduced at low temperatures. Nonetheless, even for the lowest Al content  $x = 0.16$ , an increasing resistivity with decreasing temperature was still observed. A magnetic transition remains present in all compounds at low temperatures, appearing a weak downturn in resistivity. A very small magnetoresistance was observed under an applied field at 2 K, as shown in the inset of Figure 7. In order to estimate the band gap for these systems, the Arrhenius approach was used by plotting the resistivity  $\rho$  as  $\ln \rho$  against a temperature  $T$  axis as  $1/T$ , fitting the low-temperature part as for SNAO [20]. Here, all carriers are thermally excited across the band gap, and the electron and hole concentrations are equal. The fit using  $\rho = \rho_0 e^{E_g/kT}$  yields 1250(30) K, 394(2) K and 103(1) K for  $\text{Sr}_3\text{Ni}_{1.75}\text{Al}_{0.25}\text{O}_{7-\delta}$ ,  $\text{Y}_{0.5}\text{Sr}_{2.5}\text{Ni}_{1.75}\text{Al}_{0.25}\text{O}_{7-\delta}$  and  $\text{Y}_{0.5}\text{Sr}_{2.5}\text{Ni}_{1.833}\text{Al}_{0.166}\text{O}_{7-\delta}$ , respectively.

The crystals cleave well giving rectangle pieces, where the  $c$ -axis lies out of the plane, and the long direction is the [110] direction with dimensions of 7 x 3 x 3 mm<sup>3</sup>. Magnetic susceptibility measurements are displayed in Figure 8 for the compound with phase pure single crys-

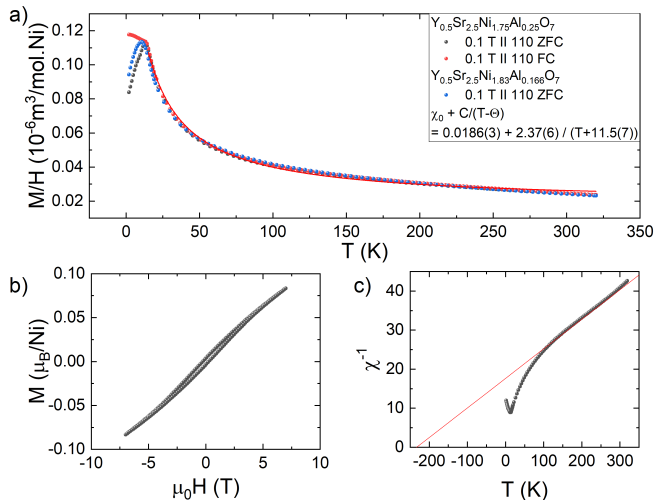


FIG. 8. Magnetic properties of a  $Y_{0.5}Sr_{2.5}Ni_{1.75}Al_{0.25}O_7$  crystal of 257 mg and a  $Y_{0.5}Sr_{2.5}Ni_{1.833}Al_{0.166}O_7$  crystal of 11 mg: a) Magnetization versus temperature at an external field of 0.1 T applied along 110 (black) and the  $c$ -axis (red). b) Magnetization versus field at 2 K for field along 110 (black) and the  $c$ -axis (red). c) Inverse magnetization versus temperature of the data in c) with Curie-Weiss fits as lines.

tals of  $x = 0.166$  and  $x = 0.25$ . Over all Al-dopings, the crystals reveal an antiferromagnetic ordering with a transition around 13 K and 11 K, and 15 K for SNAO [20]. Since AC-susceptibility showed no frequency dependence and no signal in  $\chi''$ , antiferromagnetic ordering was concluded, as previously established for SNAO [20]. Notably, with the increase in the size of the obtained single crystals, the Curie-Weiss fits can be improved with reliable masses and signals. In Figure 8 c for the  $y = 0.5$  and  $x = 0.25$  crystal, a Curie-fit with the standard linear fitting procedure for the inverse susceptibility in a range of 100-300 K is shown. This fit gives a Weiss temperatures of -240 K found along the [110] direction. The fit yields a decreased slope of  $0.07568(2)$ , resulting in a magnetic moment  $\mu_{\text{eff}} = 2.89 \mu_B$ . Considering a nominal  $Ni^{4+}$ , this cation could have a low-spin configuration with  $t_{2g}^6 e_g^0$ ,  $S = 0$ , resulting in a nonmagnetic ion, or a high-spin one with  $t_{2g}^4 e_g^2$ ,  $S = 2$ , with a corresponding expected moment of  $\mu_{\text{exp}} = 4.9 \mu_B$ . If we instead apply a Curie-fit in the whole temperature range of 15-320 K of  $\chi_0 + \frac{C}{T-\Theta}$  we find a reduced Weiss temperature of  $11.5(7)$  K. The Curie constant is reasonable with  $2.37(6)$   $\text{cm}^3 \text{K} / \text{mol.Ni}$  and the  $\chi_0$  is slightly increased from ferromagnetic impurities, which would explain the observed hysteresis. Notably, ligand-hole localization is common in transition metal oxides with unusually high valence states; in such cases, when temperature decreases, the ligand holes lose kinetic energy and localize. Future studies of low-temperature neutron diffraction on these now large high quality crystals will aim to explain the observed low magnetic moment.

## IV. SUMMARY

In conclusion, a novel doping-tuned synthesis of YSAO crystals was demonstrated, reducing the band gap, where the conductivity increased in the order of  $10^6$  for Y contents of  $y = 0.5$  and Al  $x = 0.166$ . In all cases the system shows an antiferromagnetic order below 15 K and the magnetization indicates a low moment corresponding to a  $S = 1/2$  system in contrast to the nominally expected states for a  $Ni^{4+}$  cation. TGA measurements show a wide range of Ni oxidation states dependent on the doping and oxygen content in the system, similarly to the case of rare-earth RP-type nickelate superconductors with varying  $n$ . The high crystallinity and quality of these crystals with neither polymorphism nor tetragonal-to-orthogonal transitions –characteristic of rare-earth-based systems– make them exceptional. Notably, to explore superconductivity the lowest necessary co-substitution of 8.75% Al on the Ni-site still has to be overcome. The large crystals allow for future neutron studies, which might reveal a ligand hole formation known from various high oxidation state transition metal systems possibly explaining the low moment.

## ACKNOWLEDGMENTS

We thank the Solid State Spectroscopy department for the use of their SQUID and PPMS systems.

## AUTHOR DECLARATIONS

### Conflict of Interest

The authors have no conflicts to disclose.

### Author Contributions

P.P. conceived the project, supervised the experiments and measured transport and magnetization. H.Y. grew the crystals, performed XRD, EDX and TGA measurements under the supervision of P.P. P.S.L. prepared the STEM lamella, performed the STEM measurements under the supervision of Y.E.S. The authors M.I., O.C. and P.v.A. were responsible for the project management. DFT calculations were performed by M.K. XPS samples were prepared by P.P., measured and analyzed by K.K. and U.S. The authors H.Y. and P.P. wrote the manuscript with comments from all authors.

## DATA AVAILABILITY

The data that support the findings of this study are available from the corresponding author upon reasonable request.

\* [hasan.yilmaz@imw.uni-stuttgart.de](mailto:hasan.yilmaz@imw.uni-stuttgart.de)

† [puphal@fkf.mpg.de](mailto:puphal@fkf.mpg.de)

- [1] D. Li, K. Lee, B. Y. Wang, M. Osada, S. Crossley, H. R. Lee, Y. Cui, Y. Hikita, and H. Y. Hwang, Superconductivity in an infinite-layer nickelate, *Nature* **572**, 624 (2019).
- [2] G. A. Pan, D. F. Segedin, H. LaBollita, Q. Song, E. M. Nica, B. H. Goodge, A. T. Pierce, S. Doyle, S. Novakov, D. C. Carrizales, A. T. N'Diaye, P. Shafer, H. Paik, J. T. Heron, J. A. Mason, A. Yacoby, L. F. Kourkoutis, O. Erten, C. M. Brooks, A. S. Botana, and J. A. Mundy, Superconductivity in a quintuple-layer square-planar nickelate, *Nature Materials* **21**, 160 (2021).
- [3] H. Sun, M. Huo, X. Hu, J. Li, Z. Liu, Y. Han, L. Tang, Z. Mao, P. Yang, B. Wang, J. Cheng, D.-X. Yao, G.-M. Zhang, and M. Wang, Signatures of superconductivity near 80 K in a nickelate under high pressure, *Nature* **621**, 493–498 (2023).
- [4] P. Puphal, P. Reiss, N. Enderlein, Y.-M. Wu, G. Khalullin, V. Sundaramurthy, T. Priessnitz, M. Knauff, A. Suthar, L. Richter, M. Isobe, P. A. van Aken, H. Takagi, B. Keimer, Y. E. Stuyolcu, B. Wehinger, P. Hansmann, and M. Hepting, Unconventional Crystal Structure of the High-Pressure Superconductor  $\text{La}_3\text{Ni}_2\text{O}_7$ , *Physical Review Letters* **133**, 146002 (2024).
- [5] Y. Zhu, D. Peng, E. Zhang, B. Pan, X. Chen, L. Chen, H. Ren, F. Liu, Y. Hao, N. Li, Z. Xing, F. Lan, J. Han, J. Wang, D. Jia, H. Wo, Y. Gu, Y. Gu, L. Ji, W. Wang, H. Gou, Y. Shen, T. Ying, X. Chen, W. Yang, H. Cao, C. Zheng, Q. Zeng, J.-g. Guo, and J. Zhao, Superconductivity in pressurized trilayer  $\text{La}_4\text{Ni}_3\text{O}_{10-\delta}$  single crystals, *Nature* **631**, 531 (2024).
- [6] N. Wang, G. Wang, X. Shen, J. Hou, J. Luo, X. Ma, H. Yang, L. Shi, J. Dou, J. Feng, J. Yang, Y. Shi, Z. Ren, H. Ma, P. Yang, Z. Liu, Y. Liu, H. Zhang, X. Dong, Y. Wang, K. Jiang, J. Hu, S. Nagasaki, K. Kitagawa, S. Calder, J. Yan, J. Sun, B. Wang, R. Zhou, Y. Uwatoko, and J. Cheng, Bulk high-temperature superconductivity in pressurized tetragonal  $\text{La}_2\text{PrNi}_2\text{O}_7$ , *Nature* **634**, 10.1038/s41586-024-07996-8 (2024).
- [7] J. Mitchell, J. Millburn, M. Medarde, S. Short, J. Jorgensen, and M. Fernandez-Diaz,  $\text{Sr}_3\text{Mn}_2\text{O}_7$ :  $\text{Mn}^{4+}$  Parent Compound of then=2 Layered CMR Manganites, *Journal of Solid State Chemistry* **141**, 599 (1998).
- [8] E. Castillo-Martinez and M. A. Alario-Franco, Revisiting the Sr–Cr(IV)–O system at high pressure and temperature with special reference to  $\text{Sr}_3\text{Cr}_2\text{O}_7$ , *Solid State Sciences* **9**, 564 (2007).
- [9] I. B. Sharma, C. Singh, and D. Singh, Synthesis, structure, electric transport and magnetic properties of  $\text{Sr}_3\text{MnTiO}_{7-\delta}$ , *Journal of Alloys and Compounds* **375**, 11 (2004).
- [10] M. Itoh, M. Shikano, H. Kawaji, and T. Nakamura, Structural aspects on the variations of electric and magnetic properties of the layered compound system  $\text{Sr}_{n+1}\text{V}_n\text{O}_{3n+1-\delta}$  ( $n = 1, 2, 3 \dots$ ), *Solid State Communications* **80**, 545 (1991).
- [11] S. Dann, M. Weller, and D. Currie, Structure and oxygen stoichiometry in  $\text{Sr}_3\text{Fe}_2\text{O}_{7-y}$ ,  $0 \leq y \leq 1.0$ , *Journal of Solid State Chemistry* **97**, 179 (1992).
- [12] M. M. Elcombe, E. H. Kisi, K. D. Hawkins, T. J. White, P. Goodman, and S. Matheson, Structure determinations for  $\text{Ca}_3\text{Ti}_2\text{O}_7$ ,  $\text{Ca}_4\text{Ti}_3\text{O}_{10}$ ,  $\text{Ca}_{3.6}\text{Sr}_{0.4}\text{Ti}_3\text{O}_{10}$  and a refinement of  $\text{Sr}_3\text{Ti}_2\text{O}_7$ , *Acta Crystallographica Section B Structural Science* **47**, 305 (1991).
- [13] H. Müller-Buschbaum and J. Wilkens, Ein Beitrag über  $\text{Sr}_2\text{RuO}_4$  und  $\text{Sr}_3\text{Ru}_2\text{O}_7$  zur oktaederstreckung von  $\text{M}^{4+}$  in  $\text{K}_2\text{NiF}_4$ - und  $\text{Sr}_3\text{Ti}_2\text{O}_7$ -typ-Verbindungen, *Zeitschrift für anorganische und allgemeine Chemie* **591**, 161 (1990).
- [14] Z. Li, G. Li, J. Sun, Y. Wang, L. You, and J. Lin, Structural and magnetic properties of ruddlesden–popper compounds in a double-perovskite family  $\text{Sr}_n(\text{Fe,Ta})_n\text{O}_{3n}(\text{SrO})$ , *Solid State Sciences* **8**, 1035 (2006).
- [15] Q. Li, J. Si, T. Duan, X. Zhu, and H.-H. Wen, Synthesis, structure, and physical properties of bilayer molybdate  $\text{Sr}_3\text{Mo}_2\text{O}_7$  with flat-band, *Philosophical Magazine* **100**, 2402 (2020).
- [16] I. Fukasawa, Y. Maruyama, S. Yoshida, K. Fujita, H. Takahashi, M. Ohgaki, M. Nagao, S. Watauchi, V. Gopalan, K. Tanaka, and I. Tanaka, Growth and phase transition of  $\text{Sr}_3\text{Zr}_2\text{O}_7$  single crystals, *Journal of Crystal Growth* **615**, 127241 (2023).
- [17] M. Schmidt and S. Campbell, Crystal and magnetic structures of  $\text{Sr}_2\text{Fe}_2\text{O}_5$  at elevated temperature, *Journal of Solid State Chemistry* **156**, 292 (2001).
- [18] I. B. Sharma and D. Singh, Preparation and study of structural electrical and magnetic properties of  $\text{La}_2\text{SrFe}_2\text{O}_7$  and  $\text{La}_2\text{SrMn}_2\text{O}_7$ , *Proceedings / Indian Academy of Sciences* **107**, 189 (1995).
- [19] Z. Zhang, M. Greenblatt, and J. Goodenough, Synthesis, Structure, and Properties of the Layered Perovskite  $\text{La}_3\text{Ni}_2\text{O}_{7-\delta}$ , *J. Solid State Chem.* **108**, 402 (1994).
- [20] H. Yilmaz, K. Küster, U. Starke, O. Clemens, M. Isobe, and P. Puphal, Realization of a classical ruddlesden popper type bilayer nickelate in  $\text{Sr}_3\text{Ni}_{2-x}\text{Al}_x\text{O}_{7-\delta}$  with unusual  $\text{Ni}^{4+}$ , *npj Quantum Materials* **9**, 10.1038/s41535-024-00708-5 (2024).
- [21] K. Koepf and H. Eschrig, Full-potential nonorthogonal local-orbital minimum-basis band-structure scheme, *Phys. Rev. B* **59**, 1743 (1999).
- [22] J. P. Perdew and Y. Wang, Accurate and simple analytic representation of the electron-gas correlation energy, *Phys. Rev. B* **45**, 13244 (1992).
- [23] D. Zagorac, H. Müller, S. Ruehl, J. Zagorac, and S. Rehme, Recent developments in the Inorganic Crystal Structure Database: theoretical crystal structure data and related features, *Journal of Applied Crystallography* **52**, 918 (2019).
- [24] E. Owen and E. Yates, Lxvi. x-ray measurement of the thermal expansion of pure nickel, *The London, Edinburgh, and Dublin Philosophical Magazine and Journal of Science* **21**, 809 (1936), <https://doi.org/10.1080/14786443608561628>.
- [25] S. Sasaki, K. Fujino, and Y. Takéuchi, X-ray determination of electron-density distributions in oxides, *MgO*,

- MnO, CoO, and NiO, and atomic scattering factors of their constituent atoms, *Proceedings of the Japan Academy, Series B* **55**, 43 (1979).
- [26] F. E. Wang, F. A. Kanda, and A. J. King, The lithium-strontium equilibrium system, *The Journal of Physical Chemistry* **66**, 2138 (1962), <https://doi.org/10.1021/j100817a015>.
- [27] W. G. Burgers, Röntgenographische untersuchung des verhaltens von bao-sro-gemischen beim glühen, *Zeitschrift für Physik* **80**, 352 (1933).
- [28] J. D. Bernal, E. Djatlowa, I. Kasarnowsky, S. Reichstein, and A. G. Ward, The structure of strontium and barium peroxides sro<sub>2</sub> and bao<sub>2</sub>., *Zeitschrift für Kristallographie - Crystalline Materials* **92**, 344 (1935).
- [29] R. J. Meier and R. B. Helmholdt, Neutron-diffraction study of  $\alpha$ - and  $\beta$ -oxygen, *Phys. Rev. B* **29**, 1387 (1984).
- [30] H. Pausch and H. Müller-Buschbaum, Präparation von SrNiO<sub>2</sub>-einkristallen mit eben koordiniertem nickel, *Zeitschrift für anorganische und allgemeine Chemie* **426**, 184 (1976).
- [31] M. James, J. P. Attfield, and J. Rodriguez-Carvajal, Structure and Properties of the Nickel(III) Oxide Family: LnSr<sub>5</sub>Ni<sub>3</sub>O<sub>11</sub> (Ln = Y, Dy, Ho, Er, and Tm), *Chemistry of Materials* **7**, 1448 (1995).
- [32] M. Evain, F. Boucher, O. Gourdon, V. Petricek, M. Dusek, and P. Bezdicka, Incommensurate versus commensurate description of the axbx<sub>3</sub> hexagonal perovskite-type structure. sr<sub>1.2872</sub>nio<sub>3</sub> incommensurate composite compound example, *Chemistry of Materials* **10**, 3068 (1998).
- [33] A. Hjorth Larsen, J. Jørgen Mortensen, J. Blomqvist, I. E. Castelli, R. Christensen, M. Dulak, J. Friis, M. N. Groves, B. Hammer, C. Hargus, E. D. Hermes, P. C. Jennings, P. Bjerre Jensen, J. Kermodé, J. R. Kitchin, E. Leonhard Kolsbjerg, J. Kubal, K. Kaasbjerg, S. Lysgaard, J. Bergmann Maronsson, T. Maxson, T. Olsen, L. Pastewka, A. Peterson, C. Rostgaard, J. Schiøtz, O. Schütt, M. Strange, K. S. Thygesen, T. Vegge, L. Vilhelmsen, M. Walter, Z. Zeng, and K. W. Jacobsen, The atomic simulation environment—a python library for working with atoms, *Journal of Physics: Condensed Matter* **29**, 273002 (2017).
- [34] N. Fairley, V. Fernandez, M. Richard-Plouet, C. Guillot-Deudon, J. Walton, E. Smith, D. Flahaut, M. Greiner, M. Biesinger, S. Tougaard, D. Morgan, and J. Baltrusaitis, Systematic and collaborative approach to problem solving using x-ray photoelectron spectroscopy, *Applied Surface Science Advances* **5**, 100112 (2021).
- [35] Y. Cao and Y.-f. Yang, Flat bands promoted by Hund's rule coupling in the candidate double-layer high-temperature superconductor La<sub>3</sub>Ni<sub>2</sub>O<sub>7</sub> under high pressure, *Physical Review B* **109**, 1081105 (2024).
- [36] K. Lin, Q. Li, R. Yu, J. Chen, J. P. Attfield, and X. Xing, Chemical pressure in functional materials, *Chemical Society Reviews* **51**, 5351 (2022).
- [37] E. K. Ko, Y. Yu, Y. Liu, L. Bhatt, J. Li, V. Thampy, C.-T. Kuo, B. Y. Wang, Y. Lee, K. Lee, J.-S. Lee, B. H. Goodge, D. A. Muller, and H. Y. Hwang, Signatures of ambient pressure superconductivity in thin film La<sub>3</sub>Ni<sub>2</sub>O<sub>7</sub>, *Nature* **638**, 935 (2024).
- [38] M. Zinkevich and F. Aldinger, Thermodynamic analysis of the ternary la–ni–o system, *Journal of Alloys and Compounds* **375**, 147 (2004).
- [39] M. James and J. Attfield, The Structure and Properties of an Unusual New Nickel(III) Oxide: YSr<sub>5</sub>Ni<sub>3</sub>O<sub>11</sub>, *Journal of Solid State Chemistry* **105**, 287 (1993).
- [40] P. Puphal, V. Sundaramurthy, V. Zimmermann, K. Küster, U. Starke, M. Isobe, B. Keimer, and M. Heping, Phase formation in hole- and electron-doped rare-earth nickelate single crystals, *APL Materials* **11** (2023).
- [41] M. Bianchini, A. Schiele, S. Schweidler, S. Siculo, F. Fauth, E. Suard, S. Indris, A. Mazilkin, P. Nagel, S. Schuppler, M. Merz, P. Hartmann, T. Brezesinski, and J. Janek, From LiNiO<sub>2</sub> to Li<sub>2</sub>NiO<sub>3</sub>: Synthesis, structures and electrochemical mechanisms in Li-rich nickel oxides, *Chemistry of Materials* **32**, 9211 (2020).
- [42] N. Kirikova, J. Krupa, V. Makhov, and C. Severac, Xps studies of the energy band structure of three Y<sup>3+</sup>-based fluoride compounds, *Journal of Electron Spectroscopy and Related Phenomena* **122**, 85 (2002).
- [43] B.-X. Wang, S. Rosenkranz, X. Rui, J. Zhang, F. Ye, H. Zheng, R. F. Klie, J. F. Mitchell, and D. Phelan, Antiferromagnetic defect structure in LaNiO<sub>3- $\delta$</sub>  single crystals, *Physical Review Materials* **2**, 064404 (2018).
- [44] T. Tago, N. Kataoka, H. Tanaka, K. Kinoshita, and S. Kishida, XPS study from a clean surface of Al<sub>2</sub>O<sub>3</sub> single crystals, *Procedia Engineering* **216**, 175 (2017).